Published in final edited form as:

IEEE Robot Autom Lett. 2020 April ; 5(2): 2240–2247. doi:10.1109/lra.2020.2970978.

Magnetically Steered Robotic Insertion of Cochlear-Implant Electrode Arrays: System Integration and First-In-Cadaver Results

Trevor L. Bruns[1,†], **Katherine E. Riojas**[1,†], **Dominick S. Ropella**[1], **Matt S. Cavilla**[2], **Andrew J. Petruska**[3], **Michael H. Freeman**[4], **Robert F. Labadie**[4], **Jake J. Abbott**[2], **Robert J. Webster III**[1]

[1]Department of Mechanical Engineering, Vanderbilt University, Nashville, TN, USA

[2]Department of Mechanical Engineering, University of Utah, Salt Lake City, UT, USA

[3]Department of Mechanical Engineering, Colorado School of Mines, Golden, CO, USA

[4]Department of Otolaryngology, Vanderbilt University Medical Center, Nashville, TN, USA

Abstract

Cochlear-implant electrode arrays (EAs) must be inserted accurately and precisely to avoid damaging the delicate anatomical structures of the inner ear. It has previously been shown on the benchtop that using magnetic fields to steer magnet-tipped EAs during insertion reduces insertion forces, which correlate with insertion errors and damage to internal cochlear structures. This paper presents several advancements toward the goal of deploying magnetic steering of cochlear-implant EAs in the operating room. In particular, we integrate image guidance with patient-specific insertion vectors, we incorporate a new nonmagnetic insertion tool, and we use an electromagnetic source, which provides programmable control over the generated field. The electromagnet is safer than prior permanent-magnet approaches in two ways: it eliminates motion of the field source relative to the patient's head and creates a field-free source in the power-off state. Using this system, we demonstrate system feasibility by magnetically steering EAs into a cadaver cochlea for the first time. We show that magnetic steering decreases average insertion forces, in comparison to manual insertions and to image-guided robotic insertions alone.

Keywords

Medical Robots and Systems; Surgical Robotics: Steerable Catheters/Needles

I. Introduction

Cochlear implants are among the most successful neuroprosthetic devices, restoring hearing to over 600,000 deaf or partially deaf people worldwide [1], [2]. Traditionally, the cochlear-implant electrode arrays (EAs) are inserted manually into the scala-tympani (ST) chamber of the cochlea [3], with insertion technique varying between surgeons (e.g., forces, speeds,

t.bruns@vanderbilt.edu .

†T. L. Bruns and K. E. Riojas contributed equally to this work.

angle of approach) [4]. Intracochlear trauma occurs frequently, which impairs residual hearing, increases the stimulation currents required, and results in more crosstalk between electrodes and nerves, reducing implant performance [5], [6].

Reducing trauma has been shown to help preserve residual low-frequency hearing capability and can lead to improved speech perception [7]. Preserving residual hearing is also increasingly important for electroacoustic stimulation strategies, which combine a cochlear implant with an acoustic hearing aid [8], [9]. Trauma reduction can also simplify cochlear revision procedures by reducing the amount of intracochlear ossification and fibrosis [10], [11].

Robotic approaches to EA insertion have been an area of focus for some time, since they offer greater precision in insertion technique, which may lead to less traumatic insertions [12]. Zhang *et al.* developed a direct kinematics calibration method using mechanics-based models [13], and showed that variability can be decreased using robot-assisted insertion and optimized path planning, and that robots enable insertion speed and other desired parameter values to be more easily reproduced [14]. Pile *et al.* developed a parallel robot with three degrees of freedom (DOF) to insert precurved arrays using the advance-off-stylet technique [15]. They showed that the robot could maintain insertion forces below 80mN in a cochlea phantom throughout the insertion and confirmed many of the aforementioned benefits of a robotic insertion approach. Pile *et al.* also provided workspace and parameter requirements for robotic insertion. Image guidance approaches have been shown to decrease the invasiveness of the surgical procedure and provide an optimal insertion vector for array placement [16], [17]. In particular, Caversaccio *et al.* clinically demonstrated a safe and effective robotic approach for drilling a direct access tunnel to the cochlea [17]. These works demonstrate the benefits of automation in cochlear implant surgery and motivate developing an automated tool that enables the surgeon to automatically insert the EA along the optimally planned trajectory, in a clinical setting.

Prior EA insertion tools have used a variety of innovative mechanisms of gripping and carrying EAs along the desired path. These methods include: utilizing a blunt pin and linear motion through a slotted tube [18], [19], using two titanium tube halves and manually inserting the array [17], using a gripper with two arms rotating around a pivot point to grasp the array [20]–[22], and utilizing a collet-style gripper and a parallel robot to guide array insertion [15].

Going beyond robotic insertion, steering (i.e., bending of the EA tip) has the potential to further reduce intracochlear trauma by reducing forces between the EA and the ST walls and avoiding tip impingement. Steering may also enable deeper insertions, which may enable the patient to perceive lower-frequency sounds than would otherwise be possible [23]. An EA steering method, developed by our group, utilizes a magnetic field source adjacent to the patient's head to steer a magnet-tipped EA inside of the ST and reduce insertion forces. This concept was first introduced in [24], where a benchtop system used a permanent magnet—which could be rotated with one DOF to change the applied-field direction, and translated with one DOF to change the applied-field strength—to steer a 3:1 scaled EA-like device in a 3:1 scaled ST phantom. A similar system was later evaluated using commercially

available EAs with a magnet embedded in the tip [25], inserted into improved 1:1 scale ST phantoms [26], where a significant decrease in insertion forces was reported compared to robotic insertion without magnetic steering.

In this paper, we present a complete system (see Fig. 1) that represents the culmination of prior work by our group on subsystems and algorithms [24]–[31] for magnetically steered robotic insertion of EAs. The goal of the current system is to bridge the gap between the benchtop and practical animal and cadaver experiments. Specific new contributions in this paper include: 1) introducing the first fully nonmagnetic automated insertion tool, with a novel slotted-tube approach to controllably release tapered flexible EAs after insertion, 2) incorporating silhouette-based image guidance for practical, accurate insertion-tool and magnet alignment to a preoperative plan in the operating room, which has never before been described in an archival publication, 3) replacing the moving permanent-magnet field source with a safer, stationary Omnimagnet [32] electromagnetic source, 4) introducing a stronger, cubic-core Omnimagnet, and 5) the first demonstration of magnetically steering an EA in a cadaveric specimen, verifying that force reductions shown previously in phantom models translate to the cadaver setting.

II. System Hardware and Workflow

An overview of the robotic system is shown in Fig. 1. A basic overview of the workflow with the proposed system is as follows. We first generate a patient-specific plan using the patient's preoperative computed-tomography (CT) scan. This preoperative plan includes 1) generating an optimal insertion vector and corresponding insertion-tool pose (position and orientation), 2) calculating the Omnimagnet pose that corresponds to the plan, and 3) registering the planned magnetic field vectors to the individual's ST (and the corresponding Omnimagnet coil currents to produce these vectors). Using this preoperatively generated plan, the surgeon will manually align the counterbalanced automated insertion tool and the counterbalanced Omnimagnet, and lock them in place. Both devices are optically tracked, enabling users to precisely align them using a custom image-guidance extension in 3D Slicer [33], [34]. The surgeon will then simply hold a button to run the prescribed trajectory that synchronously coordinates insertion depth and magnetic field to produce a smooth, atraumatic insertion. When insertion is complete, the Omnimagnet is powered off and the insertion tool is removed. The Omnimagnet, insertion tool, and force sensor interface with one another using custom Robot Operating System (ROS) nodes [35]. In the following sections, we describe the system components including the Omnimagnet and the new automated insertion tool for EA advancement and deployment.

A. Omnimagnet

Magnetically steering the EA through the spiral-shaped cochlea requires strong, controllable magnetic fields. Our prior work has exclusively considered a permanent magnet as the field source [24], [25]. However, as noted in [28], it may be desirable to use an electromagnetic source for three reasons: First, an electromagnet has a controllable magnetic dipole, meaning that it does not need to be physically moved during EA insertion to vary the field strength at the cochlea, eliminating any potential risk of collision with the patient or other objects.

Second, an electromagnet can be turned off and is inert when not in use, making handling, storage, and use of ferrous surgical equipment safer. Third, the relatively short duration of a surgical EA insertion (less than 30 seconds) would allow high levels of current to be sourced through the coils without reaching unsafe temperatures.

In the system presented in this paper, we have replaced the permanent-magnet source with an Omnimagnet electromagnetic source [32]. An Omnimagnet comprises three nested orthogonal coils and a ferromagnetic core. Three control inputs (the current in each coil) provide control of the magnetic dipole of this magnetic field source, which can be used to generate a desired magnetic field vector $\boldsymbol{B}$ at an arbitrary location in space. In the original conception of the Omnimagnet [32], and all prior embodiments, the ferromagnetic core was spherical. In this paper, we re-optimized the Omnimagnet for a cubic core, which has the effect of increasing the achievable dipole strength by approximately 35% for a given overall package size and current density. Our prototype cubic-core Omnimagnet has overall cubic dimension of approximately 200 mm, with a ferromagnetic cubic core of dimension 102 mm, with the dimensions of the individual coils (and their electrical resistances) provided in Table I. The Omnimagnet uses 16AWG square-cross-section copper magnet wire (MWS Precision Wire Industries, Westlake Village, CA). Our final prototype is 22 kg, which is passively supported by a lockable counterbalanced arm (Dectron, Wilsonville, OR).

As described in [32], the control equation for an Omnimagnet, assuming a basic dipole model, is

$$\boldsymbol{I} = \frac{2\pi}{\mu_0}\|\boldsymbol{p}\|^3 \mathbb{M}^{-1}(3\hat{\boldsymbol{p}}\hat{\boldsymbol{p}}^T - 2\mathbb{I})\boldsymbol{B}. \quad (1)$$

where $\boldsymbol{I}$ (units A) is the 3×1 array of coil currents, $\boldsymbol{p}$ (units m) is the vector from the center of the Omnimagnet to the desired point in space at which a desired magnetic field vector $\boldsymbol{B}$ (units T) is to be generated, $\mathbb{M}$ is a linear transformation that maps the current array $\boldsymbol{I}$ to the Omnimagnet's dipole moment $\boldsymbol{m}$ (units $\mathrm{A{\cdot}m^2}$), $\hat{p} \equiv \boldsymbol{p}/\|\boldsymbol{p}\|$, $\mu_0 = 4\pi \times 10^{-7}\ \mathrm{T \cdot m \cdot A^{-1}}$ is the permeability of free space, and I is the 3 × 3 identity matrix.

To utilize the Omnimagnet, a high-voltage DC supply powers three servo drive amplifiers (ADVANCED Motion Controls, Camarillo, CA), which regulate the current through each coil of the Omnimagnet. The amount of current is set via analog inputs (±10V). Custom control boards receive commands over Ethernet from our custom ROS nodes and generate the required analog voltage signals for each servo drive. To determine the current scaling for each coil, a certified calibrated 3-axis magnetic field sensor (3MTS, Senis, Zug, Switzerland) was used to experimentally measure the magnetic field and compare to (1).

As an additional layer of safety, we have implemented a dedicated microcontroller to monitor thermocouples embedded throughout the Omnimagnet, which shuts off the amplifiers if predefined temperature thresholds are exceeded. This microcontroller also monitors the temperature between insertion trials, which enables us to verify that the Omnimagnet has sufficiently cooled down before running another experiment.

It is important to address the safety of placing the Omnimagnet (or any strong magnetic source) near the patient's head. Strong magnetic fields are commonly used in medical diagnosis and treatment, such as Magnetic Resonance Imaging (MRI) and Transcranial Magnetic Stimulation (TMS), and a wide variety of magnetically driven medical devices have been developed [36], [37]. Safety limits for magnetic fields are based on the nature of the magnetic field, which is typically classified as: static fields, time-varying gradient fields (100 to 1000 Hz), and radiofrequency (RF) fields (10 to 100 MHz) [38]–[40]. According to the FDA's Criteria for Significant Risk Investigations of Magnetic Resonance Diagnostic Devices (2014), a static field producing less than 8 T is considered a nonsignificant risk in adults and children over the age of one month. Other sources specify that static field exposure to the head should be limited to 2 T to ensure patient comfort [38], [39]. Our research in magnetic steering of EAs currently utilizes quasistatic fields of less than 100mT, which is well below the safety limits imposed by the FDA, or recommended by other researchers. Therefore, it does not seem that the magnitude or rate of change of the magnetic fields used in magnetic steering of EAs poses any significant risk to a patient.

B. A New Insertion Tool Compatible with Magnetic Steering

Deploying an EA in the presence of strong magnetic fields presents unique constraints not encountered by previous designs of clinically-viable automated insertion tools: the insertion tool must not contain ferromagnetic components, and to be used clinically the insertion tool has to hold, push, and release the implant gently and controllably. To achieve both of these specifications, we designed a new insertion tool and a new grasping mechanism to interface with the EA (Fig. 2). The tool is constructed from a 3D printed plastic housing (Formlabs, Somerville, Massachusetts), two piezoelectric linear actuators (SLC-1770-L-E-NM, SmarAct, Oldenburg, Germany), Nitinol tubes/rods, and brass fasteners. Three spherical, retroreflective markers are attached to the body of the tool to create a rigid body for optical tracking.

Details of the insertion tool assembly can be viewed in Fig. 2(a). Tube parameters were chosen to accommodate the dimensions of the FLEX28 EA (MED-EL, Innsbruck, Austria), but can be easily adapted for use with other EAs. The distal end of the tool consists of three nested Nitinol tubes and rods, and an outer polyimide sheath. The innermost Nitinol rod assists with EA detachment and is attached to a linear actuator. The middle Nitinol tube has an approximately 10-mm-long slot for grasping the EA, and is attached to another linear actuator. The outer Nitinol tube has a slot spanning the length of the tube and serves as a guide for the EA during deployment. Finally, a polyimide sheath with a lengthwise slit surrounds the outermost Nitinol tube to constrain the thinner, tapered region of the FLEX28 (which tapers to a tip diameter that is less than half that of the proximal end) and to keep the much thinner tip of the flexible EA concentric with the proximal end. The absolute insertion depth limit of the tool is 46 mm, enabling insertion of the longest EAs currently available (the FLEXSOFT and Standard EAs by MED-EL are 31.5mm long [41]). EA insertion proceeds as described in Fig. 2(b).

III. Image Guidance and Patient-Specific Paths

In this section, we describe the preoperative steps for generating a magnetically steered insertion plan. We incorporate the state-of-the-art insertion trajectory algorithm to generate the planned patient-specific insertion vector, and then develop a methodology to automatically generate a full magnetic steering plan given only the patient-specific anatomy and insertion vector. Outputs of this automated planning are the aligned Omnimagnet and insertion tool position and orientation (patient-specific), as well as the magnetic field vectors along the ST (using an average cochlea model registered to the patient's ST).

A. Patient-Specific Insertion Planning

Our image-guided workflow begins by acquiring a preoperative CT scan. We then segment the inner-ear anatomy using the atlas-based approach of [29] and compute the optimal insertion vector as described in [30] (see Fig. 3). This angle and position defines the alignment of the automated insertion tool. This atlas-based segmentation has been used to segment in-vivo clinical CT scans with a mean surface error of 0.21mm [42].

Our steering method works by creating a magnetic field vector that is orthogonal to the insertion path at the current location of the magnetic tip of the EA, as depicted in the inset of Fig. 1(a). This is done in order to create a torque on the embedded magnet, to cause bending in the continuum body of the EA, and thus reduce the normal force on the ST wall. We generate this path using the equations in [26] that describe an average ST model based on anatomical data. We then register our magnetic field path to the medial axis segmented from the patient's ST.

Finally, using the shape of the experimentally determined field magnitudes in [25], we prescribe the magnetic field magnitudes to increase in a ramp-like manner (see Fig. 4). The field is zero during the initial linear portion of insertion, when there is no need for bending. Upon reaching the basal turn of the cochlea, the magnetic field turns on. As the EA is inserted deeper, and the ST curvature increases, the field ramps up to apply a larger moment to the tip of the EA. The field eventually saturates at the maximum power output of the electrical system.

B. Image Guidance

Using 3D Slicer, OpenIGTLink, and the Plus Server App [33], [34], we developed a custom GUI extension (see screenshot in Fig. 1(b)) that connects to the NDI Polaris Spectra optical tracker (Northern Digital Instruments, Ontario, Canada), which tracks and displays the movement of the insertion tool, Omnimagnet, and cochlea fixture in real time. This software functions using the same methodology in [31] but with different hardware and software implementation. The program guides the user to the correctly aligned tool pose determined in Sec. III-A by displaying the real-time position of the object (shown in red in the screenshot on Fig. 1(b)) to the desired pose (shown in a green in the screenshot of Fig. 1(b)). The user then manually manipulates each device until the tracked pose and desired pose are aligned, at which point the user locks the device in place.

IV. Experimental Methods

A. Phantom Experiments

We conducted proof-of-concept experiments in the phantom model developed in [26], which is useful because it is transparent and enables one to view the motion of the EA during insertion. Four insertions were performed using our robotic system and proposed workflow. To ensure that magnetic steering provided unique benefits in terms of reaction forces beyond those derived from robotic insertion alone, we performed experiments as follows: 1) unaided manual insertions by an experienced surgeon, 2) robotic insertions using the new insertion tool described in this paper, with image-guided pre-insertion alignment but no magnetic steering, and 3) robotic insertions with image guidance and magnetic steering. Table II shows a summary of these cases.

A 3D-printed ST phantom with a 1.2mm cochleostomy opening (Fig. 5, see [26] for details) was secured into a fixture with cyanoacrylate. This fixture was then mounted to a Nano17 Titanium force/torque transducer (ATI Industrial Automation, Apex, NC) attached to a frame with optical fiducial markers. A CT scan of this assembly was then acquired. As described in Sec. III, the preoperative scan was used to generate the insertion plan.

We filled the phantom with 0.9% saline solution before each insertion as in [25]. For manual insertions, a surgeon performed four unaided insertions with a new, unmodified FLEX28 EA, using the standard forceps that are used clinically for inserting EAs (see Fig. 6). In cases of robotic insertion, both with and without magnetic steering, a magnet-tipped FLEX28 EA was used. All magnet-tipped EAs were fabricated by MED-EL and include two cylindrical axially magnetized magnets (each 0.25mm in diameter by 0.41mm in length) embedded in silicone at the tip of the array (see inset of Fig. 1(b)). The EA was loaded into the insertion tool, and the Omnimagnet and insertion tool were aligned using image guidance according to the prescribed preoperative plan, with a maximum angular alignment error of less than 1°. The support arms were locked in place and the final poses of the tool and magnet were recorded. The insertion tool then deployed the EA at a constant velocity of 1.25 mm/s (this velocity was selected in view of a 0.5–3 mm/s range in the literature [3]).

The final insertion method followed the same procedure as robotic insertion described above, but also used magnetic steering during insertion. The magnetic field of the Omnimagnet was updated at a rate of 80 Hz. Four insertions with a robotic approach and four insertions with a robotic approach and magnetic steering were completed using the same magnet-tipped EA, alternating between using magnetic steering and robotic insertion alone. For all insertions, force measurements were acquired at a rate of 50 Hz. Since the EA tip could be visualized through the transparent phantom in these experiments, forces could be mapped to angular insertion depths using video collected during insertion at 60 fps.

B. Cadaver Experiments

The same three experimental methods used in the phantom experiments (see Table II) were also conducted with a formalin-fixed cadaver cochlea. The cochlea was secured in a fixture using paraffin wax and hot-melt adhesive. A patient-specific insertion plan was generated in the same manner previously described. Unaided manual insertions were

performed by an experienced surgeon with a new, unmodified FLEX28 EA (see Fig. 6). For image-guided robotic insertions, the automated insertion tool was aligned with a maximum angular alignment error of less than 2°. A second magnet-tipped FLEX28 EA was used to perform robotic insertion experiments, alternating between robotic insertion alone and robotic insertion combined with magnetic steering (a first-of-its-kind experiment). Workflow proceeded identically to the phantom experiments, with three insertions performed using each method. A force threshold of 125mN was enforced during robotic insertions. After insertion, the EA was released from the insertion tool as described in Sec. II-B and a postoperative CT scan was acquired.

V. Results

A comparison of the first contact point with the lateral wall of the ST with and without magnetic steering is shown in Fig. 5; this result is qualitatively consistent with the results of [25]. Mean insertion force magnitudes, $\|F\| = \sqrt{F_x^2 + F_y^2 + F_z^2}$, and the difference, $\Delta\|F\|$, in insertion forces for both phantom and cadaver experiments are shown in Fig. 7, where the shaded region around each curve indicates one standard deviation from the mean. In each case, force samples were grouped into bins and then averaged. A bin of 3° was used for phantom experiments and a bin of 0.125mm was used for cadaver experiments (since there was no direct visualization of angular depths during insertion). Diamonds mark the final depths of each individual insertion. For robotic methods this was defined as when the force increased 35mN or more over 1mm of actuator travel (indicative of EA buckling); for manual insertions it was at the surgeon's discretion. A one-tailed t-test analysis (as detailed in [25]) was performed, and the depths where the null hypothesis can be rejected with 95% confidence (i.e., statistically significant force reduction) are indicated with rings. All force reductions observed after the magnetic field was turned on (approximately 140° for phantom insertions, 8.0mm for cadaver insertions) were statistically significant. Compared to robotic insertion alone, magnetic steering reduced forces by an average of 53.8% during phantom insertions and 48.8% during cadaver insertions.

The forces recorded during manual insertions in cadaver are shown in Fig. 8. Note that the force data for the manual cadaver insertions is plotted vs. time since the surgeon is inserting into opaque bone, and there are no actuators to give position information in real-time.

Fig. 9 shows the average final angular insertion depths for each type of phantom and cadaver insertion. For phantom experiments, we see that the inclusion of magnetic steering resulted in deeper insertions on average compared to robotic-only or manual insertions. The average angular insertion depth for the manual insertions in cadavers was slightly higher than that of the other methods. Note that a force threshold cutoff was not enforced in these manual insertions.

The maximum temperature rise observed for the inner, middle, and outer Omnimagnet coils was 1.6°C, 10°C, and 34°C, respectively. These values are all within the Omnimagnet's operating range. It is also important to note that the Omnimagnet is never in direct contact with the patient, and is moved away after EA insertion is complete.

In summary, in both phantom and cadaver experiments, robotic insertions were smoother (with fewer force spikes) than the manual insertions, and magnetic steering significantly reduced forces with respect to robotic insertion alone.

VI. Toward Clinical Deployment

The system described in the paper was designed to be used in experiments with live guinea pigs, and will have to be scaled up (approximately 30%) to be used as a clinical system with living humans. This is due to the increased distance between the cochlea and the applied dipole. In [28], we found the optimal placement and size of a spherical NdFeB permanent magnet (i.e., an ideal dipole-field source), based upon the magnetic field values suggested in [25] for the same embedded EA tip magnets used here. We can use this result to design an equivalent-strength (measured at the location of the cochlea) Omnimagnet. Alternatively or in addition, since the Omnimagnet can be rotated such that only two coils are required, simply removing the outermost coil and enlarging the other two would enable an increase in strength that is independent of any increase in overall size.

Note also that the magnetic torque that can be generated on the magnet-tipped EA is a product of the applied field magnitude and the strength of the permanent-magnet embedded in the tip of the EA (which is proportional to its volume). When we consider that volume scales cubically with length, we conclude that substantial increases in torque can be achieved with even modest increases in the size of the embedded magnet, which are possible, since the magnets used in this paper took up less than 40% of the cross-sectional area of the EA's tip. Such an increase may preclude the need for any size increase of the Omnimagnet.

We performed a conservative sensitivity analysis to registration errors of the dipole-field source (i.e., the Omnimagnet) with respect to the cochlea. We expect a worst-case 3.2% error in field magnitude and 1.7° error in field direction due to a 1mm error in Omnimagnet position. We expect a worst-case 1.3% error in field magnitude and 2.0° error in field direction due to a 1° error in the Omnimagnet dipole $\boldsymbol{m}$. These values should be insensitive to changes in the size of the field source.

However, we also found that the dipole model used in (1) has non-negligible error in the region of interest. In the future, a calibrated model that includes the first three terms of the magnetic-field expansion (the dipole term being the first) could be used to reduce the modeling error to less than 1% [44]. Measuring the electrode position in real-time is challenging because many of the traditional sensing methods used in robotics (e.g., EM/optical tracking) either require line of sight, lack the necessary accuracy, or are too large to integrate. Future work could incorporate novel sensing methods to enable closed-loop control.

VII. Conclusion

We have presented a new robotic system to improve cochlear implant EA insertion. The primary goal of this system was to build upon prior benchtop proof-of-concept magnetic steering systems and transition toward a more clinically-focused design. We developed a

workflow for utilizing preoperative imaging to compute patient-specific insertion vectors and a magnetic guidance plan. Patient safety was improved by replacing an actuated permanent magnet with a static electromagnet. We also introduced the first nonmagnetic automated insertion tool, which is capable of deploying and releasing clinical EAs with a new set of tubes that accommodates tapered arrays and gently releases the implant after deployment. Accurate pre-insertion alignment of the insertion tool was achieved by incorporating image-guidance software paired with an optical tracking system. We experimentally validated the system by performing magnetically steered robotic insertions in a ST phantom and a first-of-its-kind magnetically steered robotic insertion into a cadaveric cochlea, demonstrating in both cases that magnetic steering lowers forces by approximately 50% compared to robotic insertion alone.

Acknowledgments

This work was recommended for publication by Editor Pietro Valdastri upon evaluation of the Associate Editor and Reviewers' comments. This work was supported in part by the National Institutes of Health under Award Number R01DC013168 and the National Science Foundation Graduate Research Fellowship under DGE-1445197. The authors thank Anandhan Dhanasingh of MED-EL for fabricating the electrodes used in these experiments.

References

[1]. The Ear Foundation. (2016) Cochlear implant information sheet. [Online]. Available: https://www.earfoundation.org.uk/hearing-technologies/cochlear-implants/cochlear-implant-information-sheet

[2]. Wilson BS and Dorman MF, "Cochlear implants: current designs and future possibilities," J. Rehabil. Res. Dev, vol. 45, no. 5, pp. 695–730, 2008. [PubMed: 18816422]

[3]. Pile J and Simaan N, "Characterization of friction and speed effects and methods for detection of cochlear implant electrode tip fold-over," in Proc. IEEE Int. Conf. Robot. Autom., 2013, pp. 4409–4414.

[4]. Yasin R, Dedmon M, Dillon N, and Simaan N, "Investigating variability in cochlear implant electrode array alignment and the potential of visualization guidance," Int. J. Med. Robot, p. e2009, 2019. [PubMed: 31099146]

[5]. Rebscher SJ, Hetherington A, Bonham B, Wardrop P, Whinney D, and Leake PA, "Considerations for the design of future cochlear implant electrode arrays: Electrode array stiffness, size and depth of insertion," J. Rehabil. Res. Dev, vol. 45, no. 5, p. 731, 2008. [PubMed: 18816423]

[6]. Badi AN, Kertesz TR, Gurgel RK, Shelton C, and Normann RA, "Development of a novel eighth-nerve intraneural auditory neuroprosthesis," Laryngoscope, vol. 113, no. 5, pp. 833–842, 2003. [PubMed: 12792319]

[7]. Dalbert A, Huber A, Baumann N, Veraguth D, Roosli C, and Pfiffner F, "Hearing preservation after cochlear implantation may improve long-term word perception in the electric-only condition," Otol. Neurotol, vol. 37, no. 9, pp. 1314–1319, 2016. [PubMed: 27579834]

[8]. Mistrík P, Jolly C, Sieber D, and Hochmair I, "Challenging aspects of contemporary cochlear implant electrode array design," World Journal of Otorhinolaryngology-Head and Neck Surgery, 2018.

[9]. Wardrop P, Whinney D, Rebscher SJ, Roland JT Jr, Luxford W, and Leake PA, "A temporal bone study of insertion trauma and intracochlear position of cochlear implant electrodes. i: Comparison of nucleus banded and nucleus contour™ electrodes," Hearing research, vol. 203, no. 1–2, pp. 54–67, 2005. [PubMed: 15855030]

[10]. Somdas MA, Li PM, Whiten DM, Eddington DK, and Nadol JB Jr, "Quantitative evaluation of new bone and fibrous tissue in the cochlea following cochlear implantation in the human," Audiology and Neurotology, vol. 12, no. 5, pp. 277–284, 2007. [PubMed: 17536196]

[11]. Ryu KA, Lyu A-R, Park H, Choi JW, Hur GM, and Park Y-H, “Intracochlear bleeding enhances cochlear fibrosis and ossification: an animal study,” PloS one, vol. 10, no. 8, p. e0136617, 2015. [PubMed: 26308864]

[12]. Majdani O, et al. , “Force measurement of insertion of cochlear implant electrode arrays in vitro: comparison of surgeon to automated insertion tool,” Acta oto-laryngologica, vol. 130, no. 1, pp. 31–36, 2010. [PubMed: 19484593]

[13]. Zhang J, Bhattacharyya S, and Simaan N, “Model and parameter identification of friction during robotic insertion of cochlear-implant electrode arrays,” in Proc. IEEE Int. Conf. Robot. Autom., 2009, pp. 3859–3864.

[14]. Zhang J, Roland JT, Manolidis S, and Simaan N, “Optimal path planning for robotic insertion of steerable electrode arrays in cochlear implant surgery,” J. Med. Devices, vol. 3, no. 1, p. 011001, 2009.

[15]. Pile J and Simaan N, “Modeling, design, and evaluation of a parallel robot for cochlear implant surgery,” IEEE/ASME Trans. Mechatronics, vol. 19, no. 6, pp. 1746–1755, 2014.

[16]. Labadie RF, et al. , “Minimally invasive image-guided cochlear implantation surgery: First report of clinical implementation,” The Laryngoscope, vol. 124, no. 8, pp. 1915–1922, 2014. [PubMed: 24272427]

[17]. Caversaccio M, et al. , “Robotic cochlear implantation: surgical procedure and first clinical experience,” Acta oto-laryngologica, vol. 137, no. 4, pp. 447–454, 2017. [PubMed: 28145157]

[18]. Kratchman LB, et al. , “A manually operated, advance off-stylet insertion tool for minimally invasive cochlear implantation surgery,” IEEE Trans. Biomed. Eng, vol. 59, no. 10, pp. 2792–2800, 2012. [PubMed: 22851233]

[19]. Miroir M, Nguyen Y, Kazmitcheff G, Ferrary E, Sterkers O, and Grayeli AB, “Friction force measurement during cochlear implant insertion: application to a force-controlled insertion tool design,” Otol. Neurotol, vol. 33, no. 6, pp. 1092–1100, 2012. [PubMed: 22772019]

[20]. Hussong A, Rau TS, Ortmaier T, Heimann B, Lenarz T, and Majdani O, “An automated insertion tool for cochlear implants: another step towards atraumatic cochlear implant surgery,” Int. J. Comput. Assist. Radiol. Surg, vol. 5, no. 2, pp. 163–171, 2010. [PubMed: 20033518]

[21]. Schurzig D, Labadie RF, Hussong A, Rau TS, and Webster III RJ, “Design of a tool integrating force sensing with automated insertion in cochlear implantation,” IEEE/ASME Trans. Mechatronics, vol. 17, no. 2, pp. 381–389, 2012. [PubMed: 23482414]

[22]. Wilkening P, et al., “Evaluation of virtual fixtures for robot-assisted cochlear implant insertion,” in 5th IEEE RAS/EMBS International Conference on Biomedical Robotics and Biomechatronics. IEEE, 2014, pp. 332–338.

[23]. O’Connell BP, et al. , “Insertion depth impacts speech perception and hearing preservation for lateral wall electrodes,” Laryngoscope, vol. 127, no. 10, pp. 2352–2357, 2017. [PubMed: 28304096]

[24]. Clark JR, Leon L, Warren FM, and Abbott JJ, “Magnetic guidance of cochlear implants: Proof-of-concept and initial feasibility study,” J. Med. Devices, vol. 6, no. 3, p. 035002, 2012.

[25]. Leon L, Warren FM, and Abbott JJ, “An in-vitro insertion-force study of magnetically guided lateral-wall cochlear-implant electrode arrays,” Otol. Neurotol, vol. 39, no. 2, pp. e63–e73, 2018. [PubMed: 29315180]

[26]. Leon L, Cavilla MS, Doran MB, Warren FM, and Abbott JJ, “Scala-tympani phantom with cochleostomy and round-window openings for cochlear-implant insertion experiments,” J. Med. Devices, vol. 8, no. 4, p. 041010, 2014.

[27]. Kratchman LB, Bruns TL, Abbott JJ, and Webster III RJ, “Guiding elastic rods with a robot-manipulated magnet for medical applications,” IEEE Trans. Robot, vol. 33, no. 1, pp. 227–233, 2017. [PubMed: 29230134]

[28]. Leon L, Warren FM, and Abbott JJ, “Optimizing the magnetic dipole-field source for magnetically guided cochlear-implant electrode-array insertions,” J. Med. Robot. Res, vol. 3, no. 1, p. 1850004, 2018. [PubMed: 30009274]

[29]. Noble JH, Dawant BM, Warren FM, and Labadie RF, “Automatic identification and 3-d rendering of temporal bone anatomy,” Otol. Neurotol, vol. 30, no. 4, p. 436, 2009. [PubMed: 19339909]

[30]. Noble JH, Warren FM, Labadie RF, Dawant B, and Fitzpatrick JM, “Determination of drill paths for percutaneous cochlear access accounting for target positioning error,” in Proc. SPIE Medical Imaging, vol. 6509, 2007, p. 650925.

[31]. Bruns TL and Webster RJ III, “An image guidance system for positioning robotic cochlear implant insertion tools,” in Proc. SPIE Medical Imaging, vol. 10135, 2017, pp. 199–204.

[32]. Petruska AJ and Abbott JJ, “Omnimagnet: An omnidirectional electromagnet for controlled dipole-field generation,” IEEE Trans. Magn, vol. 50, no. 7, pp. 1–10, 2014.

[33]. Fedorov A, et al. , “3D Slicer as an image computing platform for the quantitative imaging network,” Magnetic resonance imaging, vol. 30, no. 9, pp. 1323–1341, 2012. [PubMed: 22770690]

[34]. Ungi T, Lasso A, and Fichtinger G, “Open-source platforms for navigated image-guided interventions,” Medical Image Analysis, vol. 100, no. 33, pp. 181–186, 2016.

[35]. Quigley M, et al., “ROS: an open-source robot operating system,” in ICRA workshop on open source software, vol. 3, no. 3.2. Kobe, Japan, 2009, p. 5.

[36]. Sliker L, Ciuti G, Rentschler M, and Menciassi A, “Magnetically driven medical devices: a review,” Expert review of medical devices, vol. 12, no. 6, pp. 737–752, 2015. [PubMed: 26295303]

[37]. Abbott JJ, Diller E, and Petruska AJ, “Magnetic methods in robotics,” Annu. Rev. Cont. Robot. Autom, vol. 3, pp. 2.1–2.34, 2020.

[38]. Hartwig V, Giovannetti G, Vanello N, Lombardi M, Landini L, and Simi S, “Biological effects and safety in magnetic resonance imaging: A review,” Int. J. Environ. Res. Public Health, vol. 6, no. 6, pp. 1778–1798, 2009. [PubMed: 19578460]

[39]. International Commission on Non-Ionizing Radiation Protection, “Guidelines on limits of exposure to static magnetic fields,” Health Phys, vol. 96, no. 4, pp. 504–514, 2009. [PubMed: 19276710]

[40]. Schaefer DJ, Bourland JD, and Nyenhuis JA, “Review of patient safety in time-varying gradient fields,” J. Magn. Reson. Imaging, vol. 12, no. 1, pp. 12–20, 2000.

[41]. Dhanasingh A and Jolly C, “An overview of cochlear implant electrode array designs,” Hearing Research, vol. 356, pp. 93–103, 2017. [PubMed: 29102129]

[42]. Noble JH, Labadie RF, Majdani O, and Dawant BM, “Automatic segmentation of intracochlear anatomy in conventional CT,” IEEE Trans. Biomed. Eng, vol. 58, no. 9, pp. 2625–2632, 2011. [PubMed: 21708495]

[43]. Noble JH, Majdani O, Labadie RF, Dawant B, and Fitzpatrick JM, “Automatic determination of optimal linear drilling trajectories for cochlear access accounting for drill-positioning error,” Int. J. Med. Robot, vol. 6, no. 3, pp. 281–290, 2010. [PubMed: 20812268]

[44]. Petruska AJ, Edelmann J, and Nelson BJ, “Model-based calibration for magnetic manipulation,” IEEE Trans. Magn, vol. 53, no. 7, p. 4900206, 1 2017.

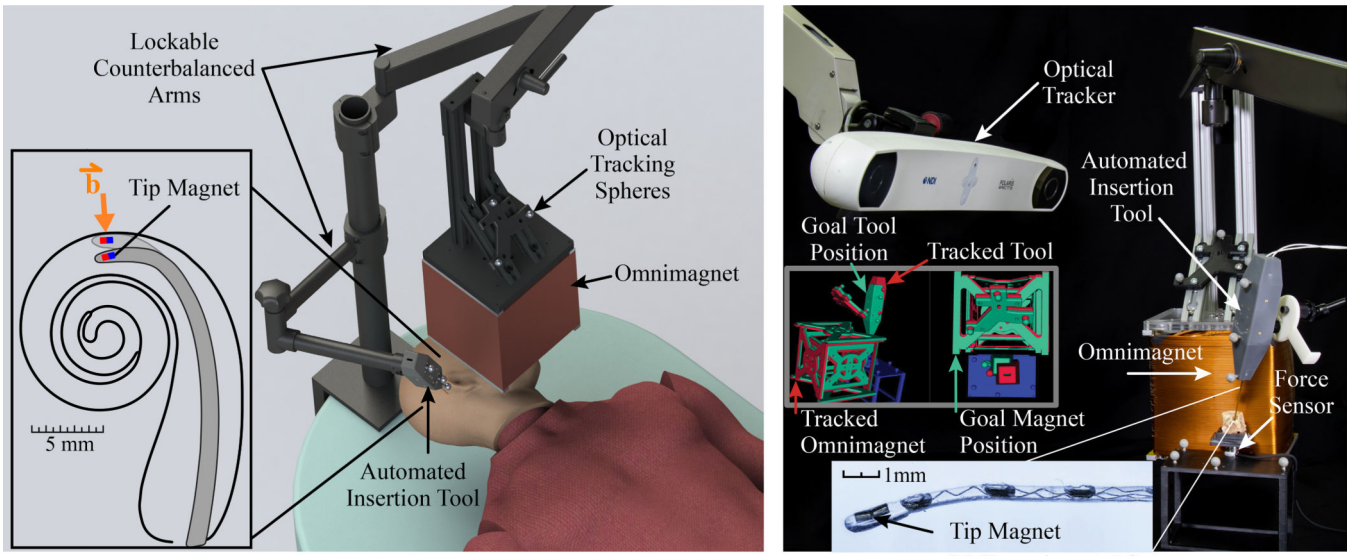

Fig. 1.

System for magnetically steered robotic insertion of cochlear-implant EAs. The automated insertion tool and Omnimagnet are both optically tracked and secured on counterbalanced positioning arms. The surgeon loads the EA into the tool and uses image guidance to align the tool and Omnimagnet with the preoperatively planned poses, at which point the arms are locked in place and the planned magnetically steered insertion trajectory is accomplished.

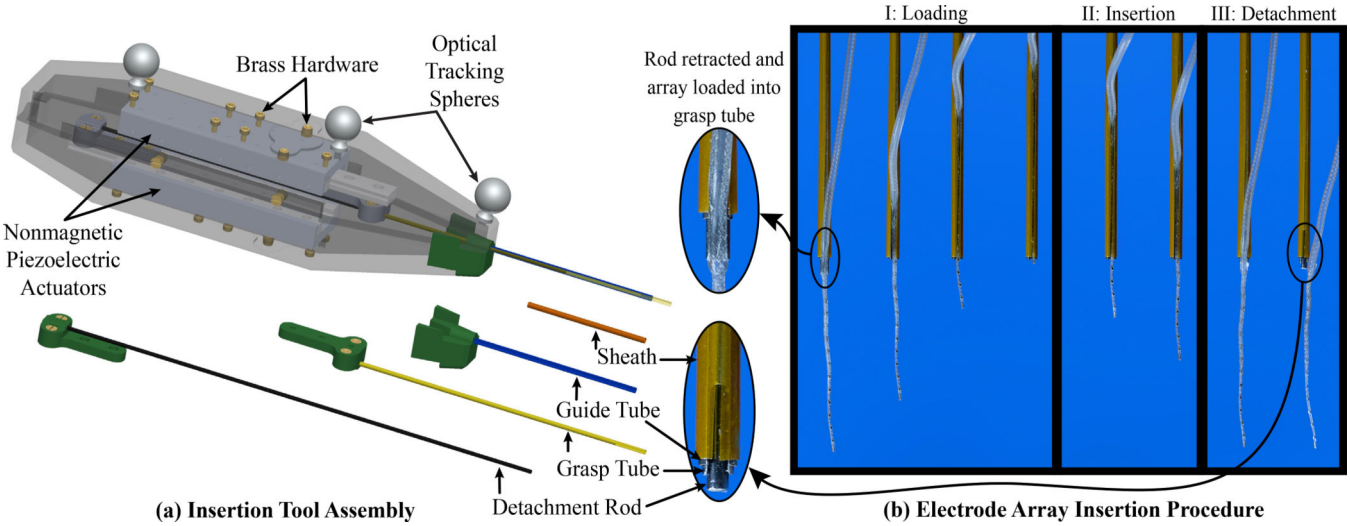

Fig. 2.

(a) Insertion tool assembly. The inner detachment rod and middle grasp tube are each attached to an actuator. The outer guide tube is connected to a detachable tip piece so that if an EA of a different diameter is to be used, it can simply be replaced with a tube of a different diameter. (b) Diagram showing tube operation for EA deployment. Step I: Loading- Load EA into the grasp tube slot and retract until the tip of the EA reaches the guide tube opening. Step II: Insertion- Insert EA by advancing the grasp tube and detachment rod simultaneously. The polyimide sheath constrains the tapered end of the EA during deployment. Step III: Detachment- Retract the grasp tube over the stationary detachment rod, which gently releases the EA from the grasp tube.

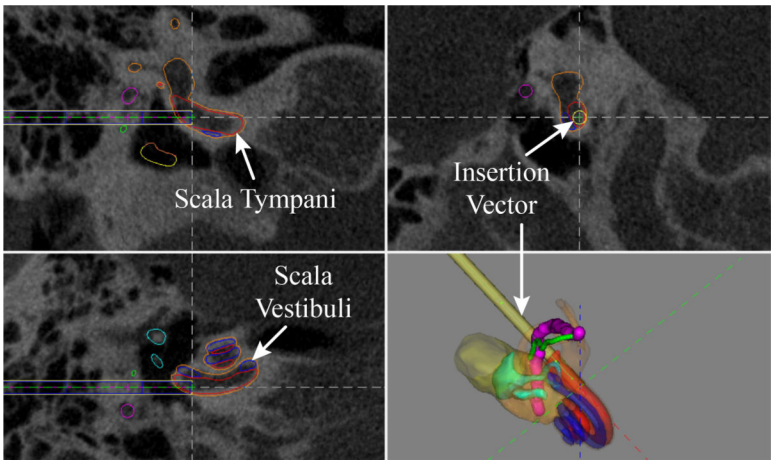

Fig. 3.
Patient-specific segmentation of cochlear anatomy and automatically generated insertion vector (yellow) [29], [42], [43].

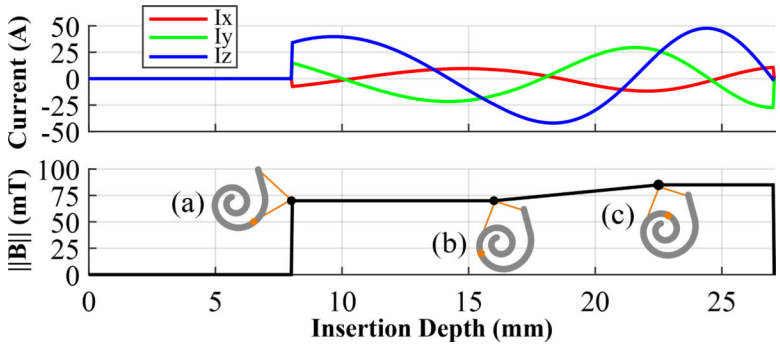

Fig. 4.

Preoperative plans for magnetic steering specify (top) the Omnimagnet coil currents required to generate (bottom) the prescribed magnetic field magnitudes based on (a) turning on the field after the initial straight insertion, then (b) ramping up the magnetic field magnitude as the ST curvature increases, until (c) saturating at the maximum power.

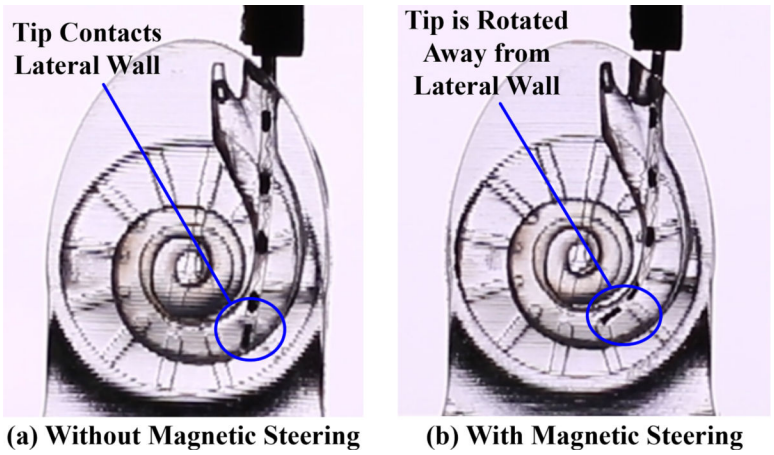

Fig. 5.

Robotic insertion into a phantom (a) without and (b) with magnetic steering. The tip of the EA is torqued away from the lateral wall in the magnetically steered case, lowering the contact force of the EA with the wall.

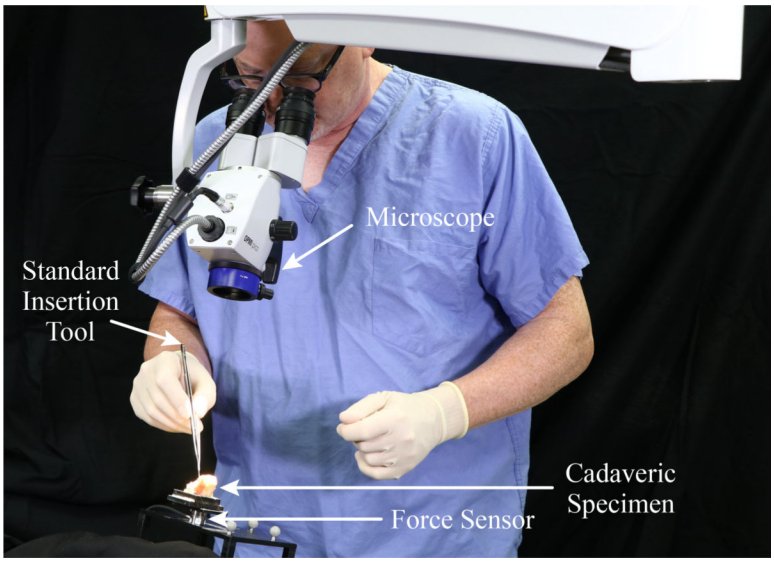

Fig. 6.
A surgeon performing a traditional EA insertion, shown here with the cadaveric cochlea.

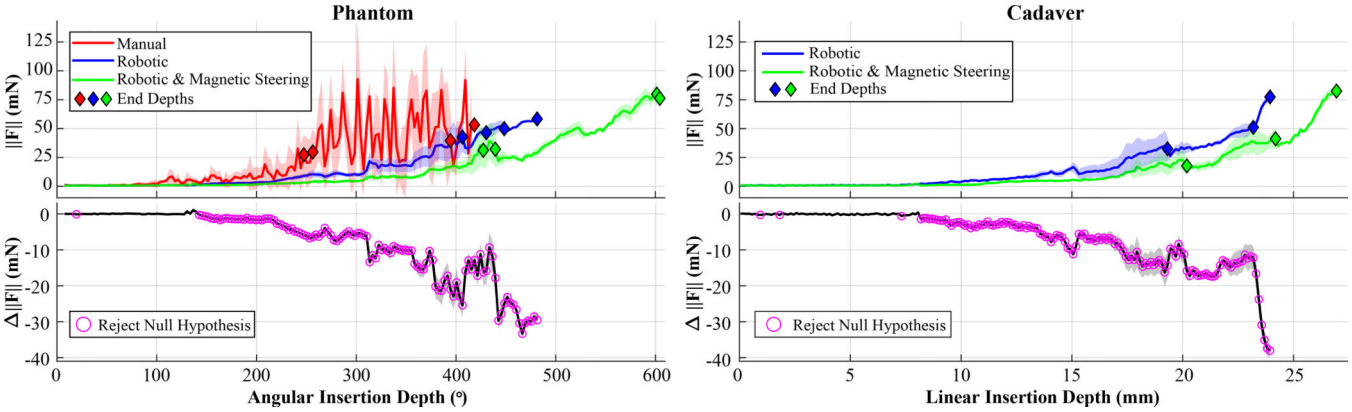

Fig. 7.

(Top) Mean insertion forces with respect to angular insertion depth for phantom experiments and linear insertion depth for cadaver experiments, illustrating that magnetic steering achieves forces that are typically lower than for robotic insertion alone. Shaded regions indicates ±1 standard deviation from the mean. Diamonds mark the final depth of each individual insertion. (Bottom) Difference in force, ΔF, between robotic insertion and magnetically steered robotic insertion. Magenta rings indicate a statistically significant decrease in force between the two methods.

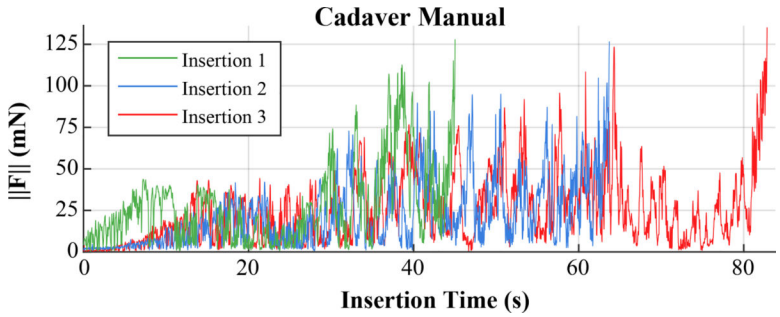

Fig. 8.

Forces observed during manual cadaver insertions exhibited more variability and larger, more frequent spikes compared to robotic methods.

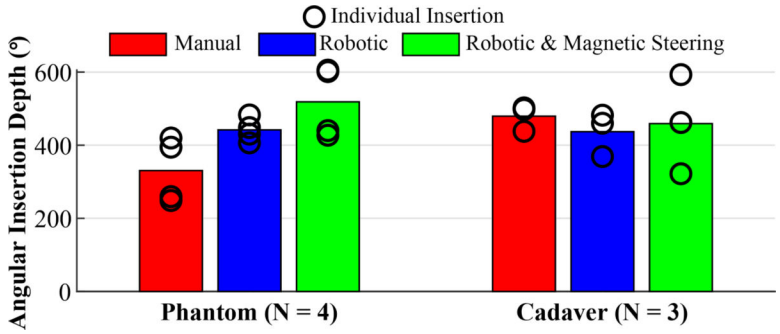

Fig. 9.

Comparison of the average final angular insertion depths for each insertion method. Depths of individual insertions are shown as black rings.

Author Manuscript

Author Manuscript

Author Manuscript

TABLE I

Properties of the Omnimagnet coils, including axial length (L), inner width (W), thickness (T), and resistance (R)

	L (mm)	W (mm)	T (mm)	R (Ω)
Inner Coil	117	105	11.2	3.5
Middle Coil	140	128	8.4	3.8
Outer Coil	154	152	6.9	4.0

TABLE II

Experimental Conditions

Method	Robotic Insertion	Image-Guided Alignment	Magnetic Steering
Manual	No	No	No
Robotic	Yes	Yes	No
Robotic & Magnetic Steering	Yes	Yes	Yes